ADVANCED FUNCTIONAL MATERIALS
www.afm-journal.de

Rationalizing Star-Shaped Nonfullerene Acceptors in Ternary Organic Solar Cells: Morphology Mediation Facilitates Exciton and Carrier Dynamics

Zhiyuan Wu, Weiyi Wang, Hui Qian, and Ziqi Liang**

Star-shaped trimeric acceptors have garnered increasing attention in organic solar cells (OSCs), yet a mechanistic gap exists on regulation of morphology and carrier dynamics. Herein, a nonfullerene acceptor named BTF-Trimer bearing a benzotrifuran core with more electronegative oxygen atoms is newly designed, which fosters intermolecular interactions with both polymer donors and small-molecule acceptors. BTF-Trimer possesses reduced aggregation tendencies and a high glass transition temperature, which are conducive to inhibiting excessive aggregation of acceptor phases and stabilizing film morphology, respectively. Notably, BTF-Trimer as morphology mediator strengthened host donor-acceptor compatibility in ternary blend active layers, forming dual-fibril interpenetrating networks that promoted exciton dissociation and hole transfer as well as alleviated bimolecular recombination in devices. Consequently, the power conversion efficiency and T_{70} (the time required to reach 70% of the initial efficiency) lifetime of the ternary OSCs in an Ar atmosphere achieved 19.13% and ≈2800 h, respectively. This study highlights the distinctive merits of star-shaped acceptors as to suppress over-crystallization and enhance phase continuity, offering insights into the interplay of phase-separated morphology and carrier dynamics, which plays a critical role in ternary devices.

1. Introduction

Organic solar cells (OSCs) are considered promising renewable energy sources thanks to their distinctive characteristics, including lightweight, semi-transparency, solution processability and large-scale manufacturing.[1–3] Recent breakthroughs of ADA′DA type non-fullerene small-molecule acceptors (SMAs) have boosted the power conversion efficiencies (PCEs) of OSCs beyond 20%, marking substantial progress toward commercial viability.[4–6] However, binary bulk-heterojunction (BHJ) SMAs-based solar cells often suffered from grand challenges in morphology regulation.[7] Remarkably, molecular disparities between polymer donors and SMAs usually led to poor compatibility during the film formation process, wherein SMAs were prone to self-assemble into oversized aggregates due to their strong crystallinity, thus generating large phase-segregation in blend films.[8,9] This is detrimental to the formation of sufficient donor (D)/acceptor (A) interfaces and continuous acceptor domains, thereby impairing exciton dissociation and charge transport. Additionally, SMAs, featuring low glass transition temperatures (T_gs), tended to diffuse rapidly within the blend films under light or heat stress, leading to severe phase-separation and device instabilities.[10–12] To tackle these morphological stability issues, researchers have implemented various methods, including molecular design,[13–17] additive engineering,[8,18] and ternary blend strategy.[19,20] Among them, incorporating oligomer acceptors (OAs) as third-components into SMAs to fabricate ternary OSCs appears an effective approach to simultaneously regulate active layer morphologies and enhance device stabilities.[21,22]

OAs, in contrast to conventional SMAs, typically consist of 2–4 repeating SMA units connected by π-linker segments. Thanks to their large molecular size and similar chemical structure as SMAs, OAs displayed high T_gs and favorable miscibility with host SMAs, which are favorable to restricting molecular diffusion motion while maintaining intermolecular packings in ternary blend active layers.[23–26] These merits allowed for ternary SMA-based OSCs to ameliorate operational stabilities whilst preserving relatively high PCEs. For example, Jen and coworkers designed and synthesized two dimeric acceptors named DYFT and DY-IDT by employing thiophene and indendithiophene (IDT) as linker units, respectively, both of which were added into the D18:BTP-eC9 binary devices to correlate linker-induced conformation lock with the stabler morphology and reduced energy losses.[24] This is due to the fact that the planar S-shaped DY-IDT was more

Z. Wu, Z. Liang
Department of Materials Science
Fudan University
Shanghai 200433, China
E-mail: zqliang@fudan.edu.cn
W. Wang, H. Qian
Research Center for Molecular Recognition and Synthesis
Department of Chemistry
Fudan University
Shanghai 200433, China
E-mail: qian_hui@fudan.edu.cn
The ORCID identification number(s) for the author(s) of this article can be found under https://doi.org/10.1002/adfm.202506436

DOI: 10.1002/adfm.202506436

conducive to forming a compact and ordered stacking with the host acceptor BTP-eC9, thus creating a distinct dual-fibril network, which promoted exciton dissociation and suppressed nonradiative recombination. Similarly, Ge and coworkers introduced two U-shaped dimeric acceptors with IDT linkers of varied molecular lengths into the binary OSCs.[25] Besides optimizing the morphology and photovoltaic properties, the thermal stabilities of 5-IDT-treated ternary devices were enhanced significantly, with maintaining 75% of its initial PCE after 1000 h of heating at 65 and 100 °C, which was ascribed to the high T_g of dimeric 5-IDT. Nonetheless, it should be noted that OAs mostly exhibited linear planar π-conjugated backbones, thereby maintaining a strong tendency to self-aggregation and hence hindering precise modulation of the D:A miscibility and film morphology during thin-film formation.[27–29]

We recently pioneered in coining star-shaped triple-branched polymeric acceptor PYTT in all-polymer OSCs, characteristic of a C_{3h}-symmetric benzotrithiophene (BTT) π-core coupled with three paradigm 2,2′-((2Z,2′Z)-((12,13-bis(2-octyldodecyl)-3,9-diundecyl-12,13-dihydro-[1,2,5]thiadiazolo[3,4-e]thieno[2″,3″:4′,5′]thieno[2′,3′:4,5]pyrrolo[3,2-g]thieno[2′,3′:4,5]thieno[3,2-b]indole-2,10-diyl)bis(methaneylylidene))bis(5-bromo-3-oxo-2,3-dihydro-1H-indene-2,1-diylidene))dimalononitrile (Y-OD) SMA units.[30] These emerging star-architecture acceptors possessed 3D channels and high molecular weights, enabling efficient electron transport and excellent operational stabilities. This has sparkled considerable research efforts. Initially, Wei, Zou, Kim and their coworkers expanded to synthesize star-shaped trimeric acceptors by connecting the BTT units with slightly modified Y-OD-based monomers.[31–33] For instance, Wei and coworkers reported such a G-Trimer that displayed a temperature-dependent aggregation property during thin-film casting. This property assisted in relaxing disordered entanglements of pre-aggregated PM6 and promoting a low energetic disorder fibrous morphology in the active layer. Later researches further broadened the family of star-shaped trimeric acceptors, comprising both fused-core[34,35] and non-fused-core types.[36,37] Notably, most of these aforementioned star-shaped trimeric acceptors shared one unique characteristic, that is, an alleviated tendency to self-aggregate due to their relatively amorphous structure compared to SMAs. This attribute is favorable for regulating excessive phase-separation yet adversely impacting charge transport even though the multi-directional channels could compensate for some of transport loss, which restrains further photovoltaic improvements.

Following the original hyperbranched PYTT research, we subsequently substituted the sulfur atom of BTT core with an oxygen atom in benzotrifuran (BTF) π-bridge to synthesize a derivative PYBF acceptor.[38] It was found that the analogous star-branched PYBF exhibited more crystalline but relatively isolated phases, which however tended to entangle with linear PYIT domains in ternary blend films due to their better miscibility than with PM6 donor. Intriguingly, this yielded neuron-like interpenetrated morphologies that favored to facilitate exciton dissociation and charge transport. Our finding motivated us to wonder whether star-shaped OAs possess similar morphology mediation in ternary OSCs. When surveying the literature, we found two recent researches conducted by Chen,[39] Li,[40] and their co-workers who attempted to incorporate star-shaped acceptors (3BTT6F and T-Alkyne-YF) as third-components into PM6:L8-BO and D18:N3 binary systems, respectively. The results showed that the PCEs of these devices were notably improved from 18.53% to 19.26% and 18.39% to 19.52%, manifesting the star-shaped acceptor's distinct capability of ameliorating morphology and performance. Still, it remains elusive how star-shaped OAs as third-components navigate morphology evolution and carrier dynamics, the correlation between those two of which is key to be rationalized in ternary OSCs.

Herein, we newly developed a star-shaped trimeric acceptor, namely BTF-Trimer, by combining three Y-OD SMA units with a BTF π-linker, and included it into the PM6:L8-BO system to elucidate the guidance of morphology mediation on carrier transport dynamics. In comparison to the conventional BTT core, BTF will enhance intermolecular interactions with the host components, which help ameliorating the morphology of ternary active layers[38] (see Figure S1, Supporting Information). Note that owing to the moderate molecular planarity, the crystallization of star-shaped trimers is weakened relative to SMAs. Morphological analysis however indicated that the relatively amorphous BTF-Trimer attenuated excessive aggregation of the acceptor phases and increased the compatibility between the host donor and acceptor. This contributes to reinforcing the acceptor phase continuity and creating a dual-fibril interpenetrating network morphology, thus promoting exciton dissociation and charge transport. Furthermore, transient absorption spectra unveiled that the addition of BTF-Trimer effectively enhanced hole transfer and undermined bimolecular recombination in the ternary devices. As a result, the PCEs were elevated from 17.35% (binary) to 18.17% (ternary) in devices, which was further boosted up to 19.13% when using 2PACz as a hole transport layer (HTL). Importantly, thanks to the low diffusion coefficient of the BTF-Trimer, the self-aggregation of the SMAs during the aging process were considerably retarded, thus enhancing the device longevity under thermal stress.

2. Results and Discussion

2.1. Molecular and Packing Characteristics

In this study, chemical structures of BTF-Trimer, L8-BO and PM6 are given in **Figure 1a**, and the corresponding synthesis routes and comprehensive characterizations are provided in the Supporting Information, including a MALDI-TOF mass spectrum (Figure S2, Supporting Information). As depicted in Scheme S1 (Supporting Information), the benzotrifuran (BTF) monomer was synthesized by a three-step process according to our previous work.[38] Next, the target BTF-Trimer was synthesized via an effective Stille coupling reaction between the BTF and TTBT5508 monomers. BTF-Trimer exhibited a high decomposition temperature of over 300 °C (T_d: 5% weight loss) under an inert atmosphere (Figure S3, Supporting Information), implying prominent thermal stabilities for OSC application. Besides, BTF-Trimer molecules displayed good solubility in common solvents such as chloroform and chlorobenzene.

The optimal molecular configuration and the related energy levels of L8-BO and BTF-Trimer were initially investigated using density functional theory (DFT) calculation based on the B3LYP/6-31G(d,p) basis set.[41] All alkyl long-chains were

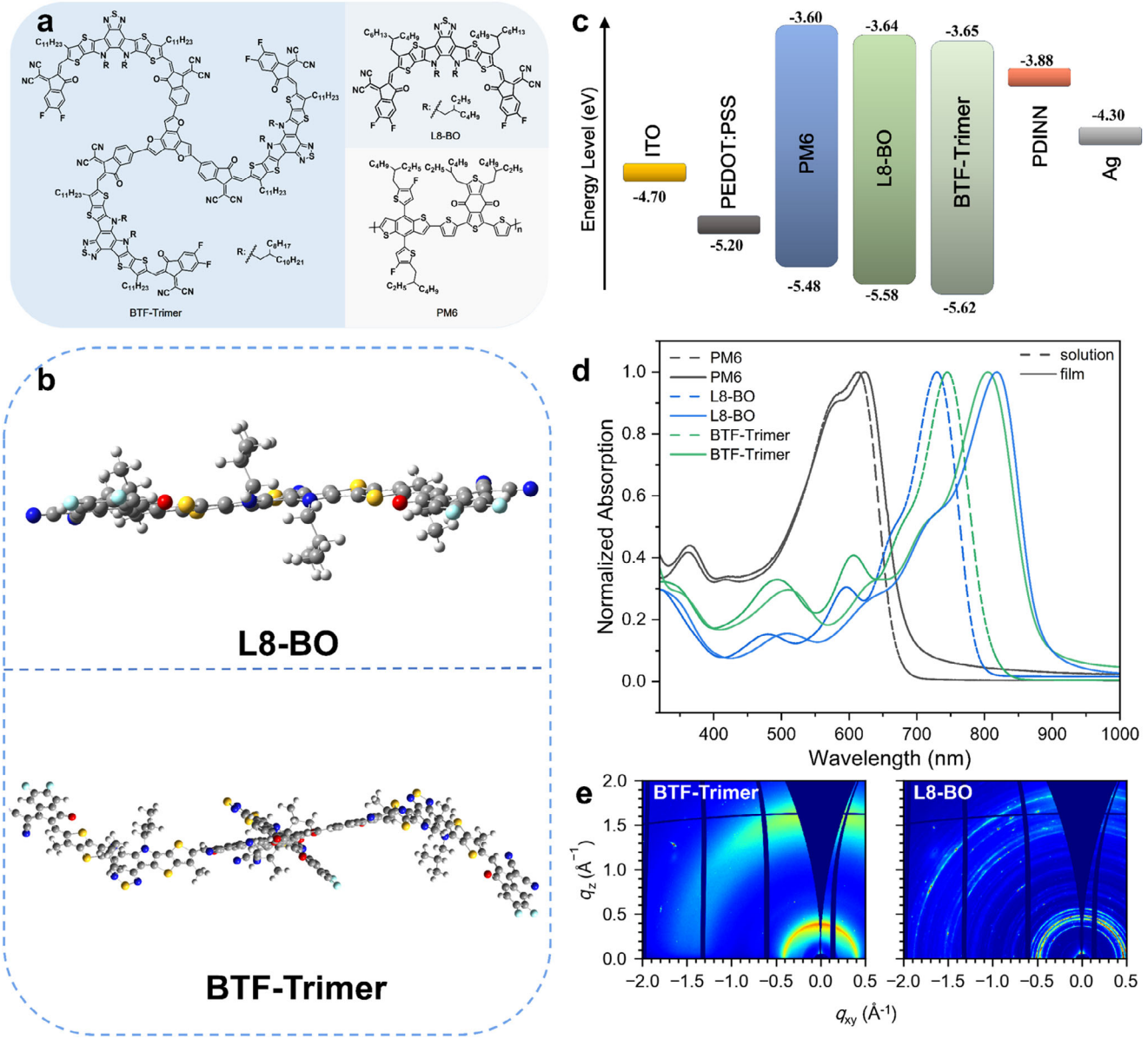

Figure 1. a) Chemical structures of BTF-Trimer, L8-BO and PM6. b) Optimized molecular conformation based on DFT simulation for L8-BO and BTF-Trimer. c) Energy level diagrams in the device. d) Normalized optical absorbance of PM6 and small-molecule acceptors in chloroform solution (dash lines) and film (solid lines). e) 2D-GIWAXS patterns of L8-BO and BTF-Trimer acceptors.

substituted by methyl groups to streamline the computations. As illustrated in Figure 1b, L8-BO displays a planar conformation, aiding in the formation of a densely compact stacking structure. In contrast to the planarized molecular conformation of L8-BO, BTF-Trimer exhibits a pinwheel-shaped structure, characteristic of an ≈20° dihedral angle between the BTF core and SMA unit, hinting a limited aggregation capacity. Also, the simulated highest occupied molecular orbital (HOMO) and lowest occupied molecular orbital (LUMO) energy levels of BTF-Trimer were estimated to be −5.56 and −3.55 eV, respectively, both of which are deeper than those of L8-BO (−5.42 /−3.41 eV), favoring the establishment of a cascade energy levels for exciton splitting in ternary OSCs. Cyclic voltammetry (CV) measurements were conducted to further validate the precision of energy levels (Figure S4, Supporting Information). As shown in Figure 1c, the LUMO/HOMO energy levels were determined to be −3.65/−5.62 eV and −3.64/−5.58 eV for BTF-Trimer and L8-BO, respectively, in good agreement with the DFT calculation.

Figure 1d displays the normalized UV–vis absorption spectra of PM6, BTF-Trimer, and L8-BO in dilute CF solution and thin films, with the corresponding optical parameters summarized in **Table 1**. L8-BO exhibited a major absorption peak centered at 729 nm in solution, whereas BTF-Trimer showed a redshifted absorption with a peak at 744 nm due to its interior star-shaped structure that facilitates the entanglements and pre-aggregation in solution.[30] Transitioning from solution to thin-film state, both

Table 1. Optical characteristics and energy levels of PM6, L8-BO and BTF-Trimer.

Material	λ_{max}^{sol}/nm [a]	λ_{max}^{film}/nm [b]	E_g/eV [c]	E_{HOMO}/eV [d]	E_{LUMO}/eV [d]
PM6	613	623	1.816	−5.48	−3.60
L8-BO	729	819	1.405	−5.58	−3.64
BTF-Trimer	744	805	1.410	−5.62	−3.65

[a] Absorption peaks in chloroform solution; [b] Absorption peaks in thin film; [c] Optical bandgaps calculated from the absorption edge of films: $E_g = 1240/\lambda_{edge}$; [d] Measured by cyclic voltammetry.

BTF-Trimer and L8-BO redshifted the absorbances with the maximum bands observed at 805 and 819 nm, respectively. The absorption onsets for BTF-Trimer and L8-BO films were located at 880 and 883 nm, corresponding to the optical bandgaps (E_g^{opt}s) of 1.410 and 1.405 eV, respectively. Notably, the 90 nm-redshift in L8-BO thin film relative to that in the solution is considerably larger than that in BTF-Trimer (61 nm), indicative of the weaker aggregation of BTF-Trimer in thin film. Furthermore, the extinction coefficient of L8-BO was determined to be 3.7×10^4 cm^{-1} at the peak maximum, higher than that of BTF-Trimer (3.3×10^4 cm^{-1}), confirming the stronger crystallization properties of L8-BO (Figure S5, Supporting Information).

To investigate the different packing behaviors of the acceptors, 2D grazing incidence wide-angle X-ray scattering (GIWAXS) images and the corresponding 1D linecuts of L8-BO and BTF-Trimer were acquired as depicted in Figure 1e and Figure S6 (Supporting Information). Both acceptors demonstrated a preferential face-on molecular packing orientation, with prominent (*010*) and (*100*) diffraction peaks in the out-of-plane (OOP) and in-plane (IP) directions, respectively. It is noteworthy that L8-BO apparently exhibited multiple diffraction rings or spots, reflecting its exceptionally high crystallinity, which might result in a mismatch in the crystallization rates between donor and acceptor, leading to excessive self-aggregation and phase-separation in binary blend films. In contrast, BTF-Trimer showed no significant diffraction rings or spots, suggestive of weaker crystallization tendencies, which favors regulating phase-segregated morphologies of the ternary blend film. Moreover, we performed the grazing incidence small-angle X-ray scattering (GISAXS) measurements (Figure S7, Supporting Information) to unravel the crystallization properties of neat acceptors. We calculated the crystalline domain size of L8-BO and BTF-Trimer by fitting the Fractal models with parameters summarized in Table S1 (Supporting Information).[42,43] It can be seen that the domain size of L8-BO neat film is larger than that of BTF-Trimer neat film (R_g = 61.7 vs 53.8 nm), corroborating the GIWAXS results.

2.2. Device Performance and Working Principles

To investigate the effect of the BTF-Trimer on device performance, binary and ternary OSCs with a conventional structure of indium tin oxide (ITO)/poly(3,4-ethylenedioxythiophene):poly(styrenesulfonate) (PEDOT:PSS)/-PM6:Acceptors/poly(diiodine nitride) (PDINN)/Ag were fabricated. Detailed device fabrication and optimization details are provided in the Experimental Section and Table S2 (Supporting Information). The current density–voltage (*J*–*V*) curves and the schematic diagram of the device structure are displayed in **Figure 2a**. As summarized in **Table 2**, the L8-BO-based binary OSCs delivered a PCE of 17.35%, with an open-circuit voltage (V_{OC}) of 0.861 V, a short-circuit current density (J_{SC}) of 26.99 mA cm^{-2}, a fill factor (FF) of 74.62%. By contrast, the BTF-Trimer-based analogous devices yielded a PCE of 17.10% with an enhanced V_{OC} of 0.927 V yet significantly reduced J_{SC} of 25.13 mA cm^{-2} and FF of 73.43%. The suppressed J_{SC} is mainly attributed to the weaker aggregation and the attenuated optical absorbance as discussed above. In contrast to the host PM6:L8-BO device, the ternary devices based on PM6:L8-BO:BTF-Trimer by a weight ratio of 1:1:0.2 presented the enhancements in both V_{OC} (0.875 V) and J_{SC} (27.15 mA cm^{-2}), thereby achieving a higher PCE of 18.17%. Furthermore, with the aid of [2-(9H-carbazol-9-yl)ethyl]phosphonic acid (2PACz) as an HTL, the ternary devices realized an excellent PCE of 19.13%. In addition, the external quantum efficiency (EQE) profiles of four devices are shown in Figure 2b, and the integrated J_{SC} values from the EQE spectra were calculated to be 25.55, 24.53, 25.62 and 26.09 mA cm^{-2}, respectively, which are well-aligned with the J_{SC} values measured from the *J*–*V* curves. Figure 2c displays Gaussian-fitted PCE distributions of these OSCs, implying that these OSCs are reproducible.

In order to unravel the mechanisms of the enhancement of device performances, the charge generation, transport, and recombination properties were investigated systematically. Figures 2d and S8 (Supporting Information) summarize the hole (μ_h) and electron (μ_e) mobilities of binary and ternary devices based on space-charge limited current (SCLC) measurements. The μ_h values of L8-BO- and BTF-Trimer-based devices were determined to be 7.61×10^{-4} and 7.36×10^{-4} cm^2 V^{-1} s^{-1}, respectively, whereas their corresponding μ_e values of were 5.27×10^{-4} and 5.22×10^{-4} cm^2 V^{-1} s^{-1}, respectively. It is interesting to note that L8-BO and BTF-Trimer possessed similar electron mobilities, even though their aggregation state structures were quite different, with L8-BO being more crystalline while BTF-Trimer more amorphous. This is mainly attributed to the fact that the triple-armed structure of the star trimer provided multiple electron channels, which reinforced electron transport and therefore compensated for the relatively poor crystallization and packing capabilities. Furthermore, after adding the BTF-Trimer as a third-component to the L8-BO-based blend film, both μ_h and μ_e values were elevated to 7.90×10^{-4} and 6.22×10^{-4} cm^2 V^{-1} s^{-1}, with a more balanced μ_h/μ_e of 1.27 than that of L8-BO-based (1.44) and BTF-Trimer-based (1.41) binary devices. The fast and balanced charge transport in the blend films led to the high J_{SC} and FF of the OSCs.

The charge generation and exciton dissociation properties were examined by steady-state photoluminescence (PL) and

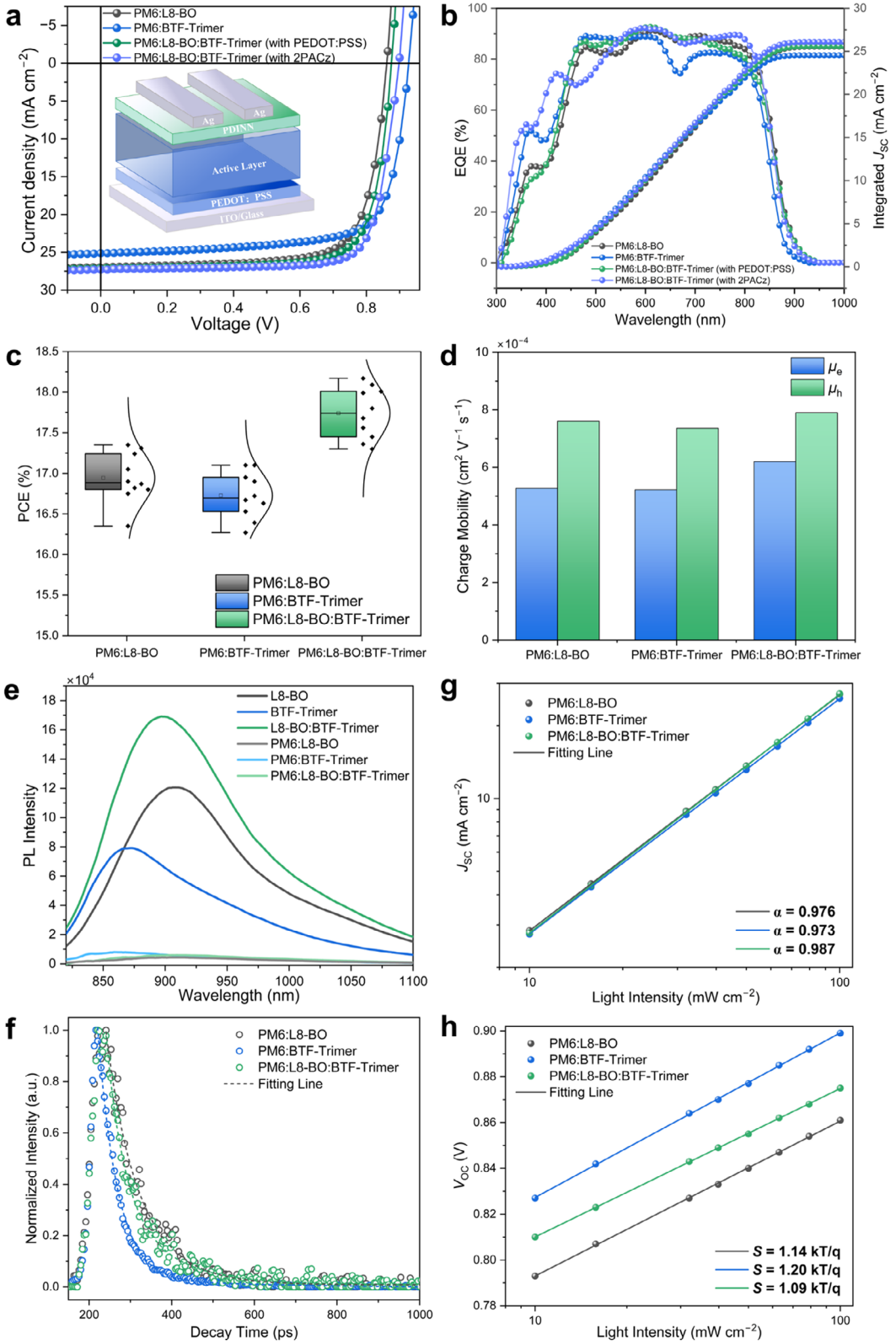

Figure 2. a) *J–V* curves of optimal devices under AM 1.5 G illumination with an inset schematic showing the device architecture. b) EQE spectra and integrated J_{SC} plots of binary and ternary OSCs. c) Statistical box plots of PCEs. d) Hole and electron mobilities of devices based on SCLC measurements. e) Steady-state PL spectra of the acceptor-only and blend films and f) TRPL decay kinetics of the binary and ternary films under 800 nm photo-excitation. Light-intensity dependences of g) J_{SC} and h) V_{OC}.

Table 2. Photovoltaic parameters of the optimal PM6:L8-BO, PM6:BTF-Trimer and PM6:L8-BO:BTF-Trimer based devices.

Devices	V_{OC} [V]	J_{SC} [mA cm^{-2}]	J_{cal} [mA cm^{-2}][a)]	FF [%]	PCE [%]
PM6:L8-BO	0.861	26.99	25.55	74.62	17.35
PM6:BTF-Trimer	0.927	25.13	24.53	73.43	17.10
PM6:L8-BO:BTF-Trimer	0.875	27.15	25.62	76.45	18.17
PM6:L8-BO:BTF-Trimer[b)]	0.898	27.30	26.09	78.05	19.13

[a)] J_{SC} values are calculated from the EQE curves; [b)] 2PACz as HTL.

time-resolved photoluminescence (TRPL) spectroscopies of single-component and blend films. As shown in Figure 2e, L8-BO and BTF-Trimer thin films exhibited comparable intensities of PL bands, that is, 1.20×10^5 and 7.90×10^4, respectively. When mixing L8-BO with BTF-Trimer, the PL peak intensity significantly rised to 1.70×10^5, indicative of more photogenerated excitons and decreased non-radiative recombination. By pairing with PM6 donor, the ternary blend film showed a higher PL quenching efficiency of 96.0% than that of L8-BO-based (95.7%) and BTF-Trimer-based (90.0%) blend films, suggesting the existence of efficient exciton dissociation. Figures 2f and S9 (Supporting Information) illustrate the TRPL decay curves and bi-exponential fitting lines for the blend and neat acceptor films, respectively. Neat L8-BO thin film displayed a PL decay lifetime of 141.9 ps, higher than that of BTF-Trimer (110.7 ps), resulting from the more crystalline microstructure of L8-BO than BTF-Trimer. When blending with PM6, the PL decay lifetime of L8-BO was reduced to 52.0 ps, whereas that of BTF-Trimer was down to 48.1 ps, implying the faster exciton dissociation process in PM6:BTF-Trimer due to the more favorable miscibility between PM6 and BTF-Trimer, thus creating more D/A interfaces, which will be rationalized in the next section. Surprisingly, upon the addition of the BTF-Trimer acceptor into the PM6:L8-BO binary system, the PL quenching process was accelerated further to 42.0 ps, suggesting that the addition of BTF-Trimer promotes exciton dissociation. Subsequently, the charge recombination mechanism in devices was revealed by the dependence of J_{SC} and V_{OC} on light intensity (P_{light}) as depicted in Figure 2g,h. The α values were found to be 0.976, 0.973 and 0.987 for the L8-BO and BTF-Trimer-based binary, and L8-BO:BTF-Trimer-based binary devices, respectively, indicating that bimolecular recombination was effectively suppressed in the optimal ternary device. Moreover, the curves of V_{OC} versus P_{light} were plotted, from which the slope of the ternary devices was calculated to be 1.09 kT/q that is the minimum value among devices, indicative of less trap-assisted recombination, which potentially contributes to their outstanding photovoltaic performances.

2.3. Dual-Fibril Interpenetrating Network

Since the above-mentioned photovoltaic and photogenerated charge properties are correlated intimately with the blend film morphologies, we systematically characterized the phase-separation and aggregate attributes of the binary and ternary blend films by employing tapping-mode atomic force microscope (TP-AFM), transmission electron microscopy (TEM), GIWAXS and GISAXS measurements (**Figure 3**). As shown in Figure 3a, the L8-BO-based and BTF-Trimer-based binary blend films displayed distinctly different surface morphologies, with L8-BO-based film featuring obvious granular aggregates and a root-mean-square (RMS) roughness of 4.013 nm, as opposed to the BTF-Trimer-based blend film, which is relatively homogeneous with an RMS roughness of 2.807 nm. After adding third-component BTF-Trimer, the RMS of the PM6:L8-BO:BTF-Trimer blend films was significantly reduced down to 2.902 nm, forming an optimal dual-fibril interpenetrating network. TEM characterization provides more intuitionistic evidence about the phase-separation morphology in the polymer blends, which accord well in with the AFM results (Figure 3b). The TEM image of PM6:L8-BO film displayed a morphology of numerous relatively isolated clusters while the binary PM6:BTF-Trimer and ternary PM6:L8-BO:BTF-Trimer blend films exhibited the enhanced acceptor domain continuity and a distinct dual-fibril network, which is more beneficial for exciton dissociation and charge transfer. To elucidate the working mechanism of the star-shaped acceptor BTF-Trimer for the formation of homogeneous phase size and enhanced phase continuity, contact angle measurements were performed to assess the compatibilities among the three components in the ternary blend, as shown in Figure S10 (Supporting Information). The surface energy (γ) values were derived from the contact angle data by the Owens model[44] and then the Flory-Huggins interaction parameters (χ) were calculated based on a formula of $\chi = K(\sqrt{\gamma_1} - \sqrt{\gamma_2})^2$ as summarized in Table S3 (Supporting Information).[45] The χ values were calculated to be 0.28, 0.075, and 0.065 K for binary PM6:L8-BO, PM6:BTF-Trimer and L8-BO:BTF-Trimer blends respectively, indicating that the BTF-Trimer possessed superior compatibilities with both PM6 and L8-BO. Therefore, BTF-Trimer served as a morphology modifier to alleviate severe phase separation in PM6:L8-BO blend films. Additionally, the location of BTF-Trimer in BHJ blends could be estimated by the wetting coefficient for the ternary BHJ blend on the basis of the interfacial surface energy (see Table S4, Supporting Information).[46,47] The wetting coefficient of BTF-Trimer was calculated to be 0.011, indicative of its location at the interface between PM6 and L8-BO. This implies that BTF-Trimer not only reduces the scale of phase separation at the donor/acceptor interfaces but also takes advantage of the better compatibility with L8-BO to reinforce phase continuity through entanglement, thus forming a bi-continuous fibril network to strengthen exciton dissociation and charge transport, as evidenced by the AFM and TEM results.

Aside from the surface morphology as discussed above, creating a homogeneous vertical phase distribution in bulk is also of vital importance to charge transport. Therefore, we carried out the film-depth-dependent light absorption spectra (FLAS) measurements (Figure S11a–c, Supporting Information) to fit the composition ratios across the vertical direction, as

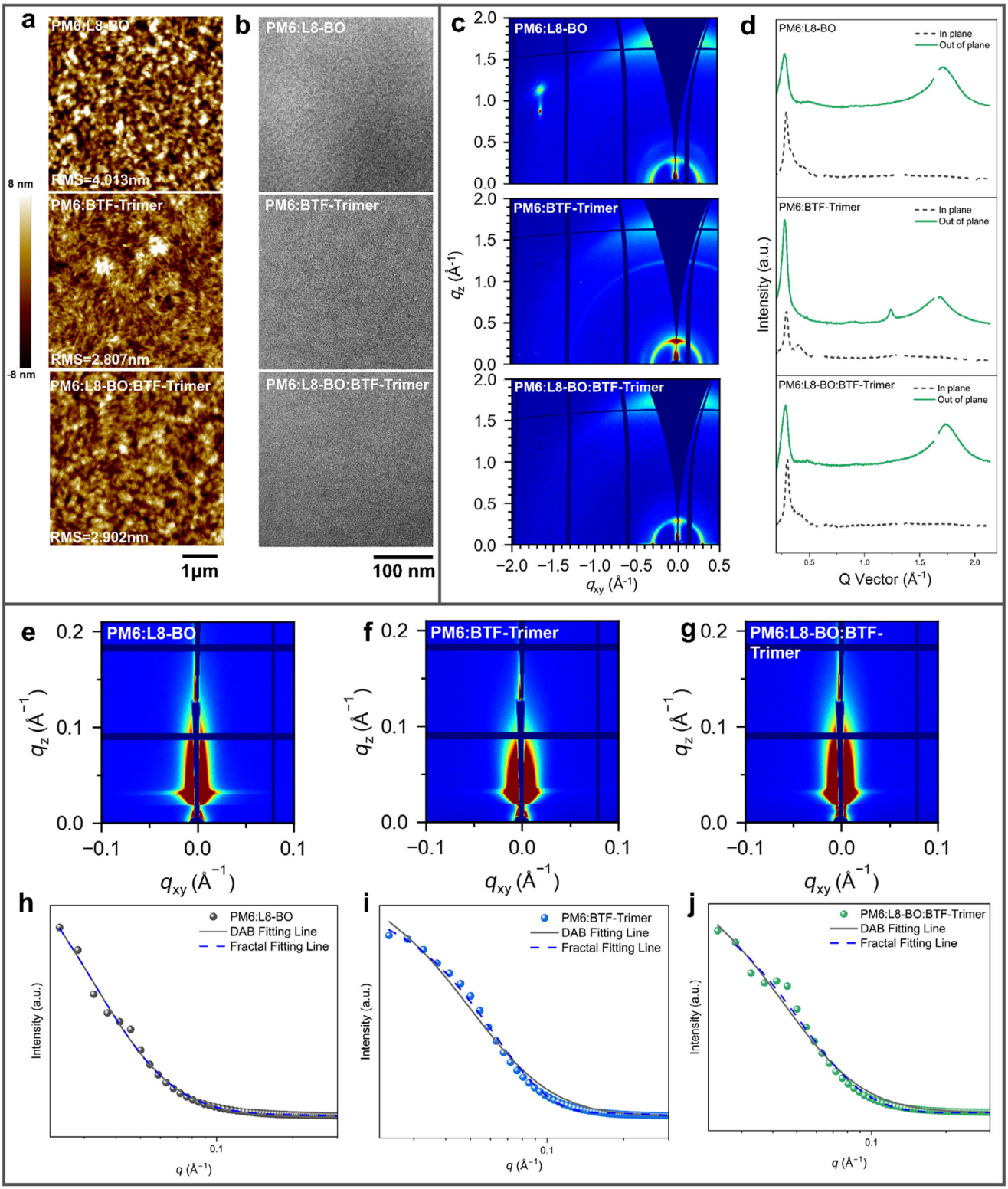

Figure 3. Morphology characterization of binary and ternary blend films. a) TP-AFM height and b) TEM images. c) 2D-GIWAXS patterns and d) the corresponding line cuts of in-plane (dash lines) and out-of-plane (solid lines) directions. 2D-GISAXS patterns of e) PM6:L8-BO, f) PM6:BTF-Trimer, and g) PM6:L8-BO:BTF-Trimer blends as well as h–j) the corresponding 1D fitting lines.

shown in Figure S11d–f (Supporting Information). It was found that the PM6:L8-BO blend exhibited a larger variation of the composition ratios than that of PM6:BTF-Trimer, in particular between 30 and 80 nm, implicative of large phase-separation in the vertical direction, thus impairing charge transport. In contrast, the variations of the composition ratios in the PM6:BTF-Trimer blend were smaller. After introducing BTF-Trimer into the PM6:L8-BO blend, the composition ratios became more homogeneous, with fluctuations above and below 50%, suggestive of the favorable vertical phase distribution. Therefore, it can be concluded that the BTF-Trimer also acted to regulate vertical phase-separated morphologies, benifiting charge transport in devices.

Furthermore, the microstructures and molecular packing behaviors were investigated by GIWAXS measurements. Figure 3c,d show the 2D GIWAXS patterns and the corresponding line cuts of IP (dash lines) and OOP (solid lines) directions of binary and ternary blend films. We notice that there was an anomalous diffraction point at $q_{xy} \approx -1.7$ and $q_z \approx 0.8-1.2$, which is assumed to arise from some impurity signals since we conducted the testing in air, yet it had limited effect on the accuracy of the results. Evidently, all the blend films displayed face-on orientations, which aid in intermolecular charge transport. Specifically, as shown in Figure S12 (Supporting Information), in the OOP direction, the L8-BO- and BTF-Trimer-based blend films showed (*010*) peaks at ≈1.71 Å^{-1} (*d*-spacing = ≈3.67 Å) and ≈1.69 Å^{-1} (*d*-spacing = ≈3.71 Å), with the corresponding crystalline coherence lengths (CCLs) of 22.1 and 17.8 Å, respectively. The tighter π–π stacking distance and the larger CCLs of L8-BO-based binary films further confirm that L8-BO possessed stronger crystallization properties, which could lead to severe phase-segregation. Besides, BTF-Trimer exhibited a diffraction peak around $q_z = 1.3$, indicative of the increased spacing distance between some molecules due to reduced molecular planarity. After adding BTF-Trimer into the PM6:L8-BO binary system, the CCLs dropped down to 20.5 Å and the diffraction peak at $q_z = 1.3$ disappeared, implying that BTF-Trimer has a good compatibility with L8-BO and can function as a morphology modifier to effectively inhibit excessive aggregation of L8-BO, in agreement with the microscopic and contact angle measurement results. Notably, despite that the CCLs in the OOP direction of ternary blend films were slightly decreased, the *d*-spacing of the ternary in the OOP direction declined to 3.61 Å, suggesting the denser π–π stacking. This is presumably ascribed to the entanglement effect of the BTF-trimer, which bridges the neighboring molecules in the acceptor phases. The IP direction exhibited the similar trend as the OOP direction, with *d*-spacings of 15.10, 15.71 and 16.36 Å for PM6:L8-BO, PM6:BTF-Trimer and PM6:L8-BO:BTF-Trimer, respectively, indicating that the over-aggregations in PM6:L8-BO were suppressed.

To quantitatively reveal the role of the BTF-Trimer on the domain sizes in blend films, GISAXS patterns of the blend films were acquired as shown in Figure 3e–g. We employed the DAB and fractal models to fit the domain size of donor and acceptor in blend films, respectively, as shown in Figure 3h–j and the corresponding fitting parameters are summarized in Table S5 (Supporting Information), where ξ represents the correlation length of PM6 domains, R_g reflects the domain size of the crystallized acceptor particles, and D is the fractal dimension of the acceptor. Note that the ξ values showed little change whereas the R_g values varied a lot among the three blend films. Specifically, the PM6:L8-BO blend exhibited much larger acceptor crystalline domain size than that of the PM6:BTF-Trimer blends (with R_g = 51.9 vs 27.5 nm), suggesting that L8-BO displayed strong self-aggregation tendencies in the blend system while BTF-Trimer possessed better compatibility with the donor. Furthermore, after introducing BTF-Trimer as a third-component into PM6:L8-BO, the domain size of the acceptor phase was decreased down to 33.1 nm. These results further establish that BTF-Trimer could behave as a morphology modifier to enhance D/A miscibility and mitigate the tendency of L8-BO to over-crystallization, thereby circumventing large-scale phase-separation.

2.4. Efficient Exciton Dissociation and Hole Transfer

With the aid of transient absorption spectroscopies (TAs), we in-depth rationalize the correlation of phase morphology on the exciton and free carrier dynamics, in particular the hole transfer and recombination processes. An excitation wavelength of 800 nm was firstly used to selectively excite the acceptors. The 2D TAs images and the corresponding spectra of the neat and blend films are shown in **Figure** 4a,b. For the neat acceptor films, the ground state bleaching (GSB) signals and excited-state absorption (ESA) signals of both acceptors were located in the range of 700–850 and 850–950 nm and the corresponding decay curves are illustrated in Figures 4c and S13a (Supporting Information), respectively. By fitting the GSB and ESA decay curves with an exponential function, L8-BO and BTF-Trimer displayed comparable exciton lifetimes of ≈9.7 ps and local excited (LE) state lifetimes of ≈12 ps. However, after mixing with donor PM6, there were noticeable differences in carrier lifetimes between binary and ternary blend films as shown in Figures 4d and S13b (Supporting Information). The GSB decay properties of different blends were estimated by fitting the dynamic curves with a bi-exponential function and the carrier lifetimes obtained were divided into τ_1 and τ_2, where τ_1 is attributed to the fast dissociation of the exciton at the D/A interface, and τ_2 is related to the diffusion of the exciton in the donor–acceptor phase. The τ_1 value of the L8-BO-based blends was fitted to be 1.16 ps, lower than that of 1.87 ps in the BTF-Trimer-based binary blends, indicative of a faster exciton dissociation process in the L8-BO-based blend thanks to the enhanced crystallization. In contrast, the τ_2 value of BTF-Trimer-based blends was determined to be 16.36 ps, shorter than that of 17.38 ps in the L8-BO-based binary blends, implying the more rapid exciton diffusion in the BTF-Trimer-based blends. This is due to the relatively weak crystallinity of BTF-Trimer and also the improved compatibility with PM6 donor, which prevented the formation of oversized and isolated domains, thereby facilitating faster diffusion of excitons to the interfaces. Furthermore, the LE state lifetimes of BTF-Trimer-based binary and ternary blend films were fitted from the ESA decay curves (Figure S13b, Supporting Information) and then calculated to be 12.38 and 16.37 ps, respectively, lower than that of L8-BO-based binary films (21.77 ps). The relatively faster decay of the LE state after introducing BTF-Trimer as a third-component into PM6:L8-BO blend films could be attributed to its efficient and rapid conversion to the delocalized singlet

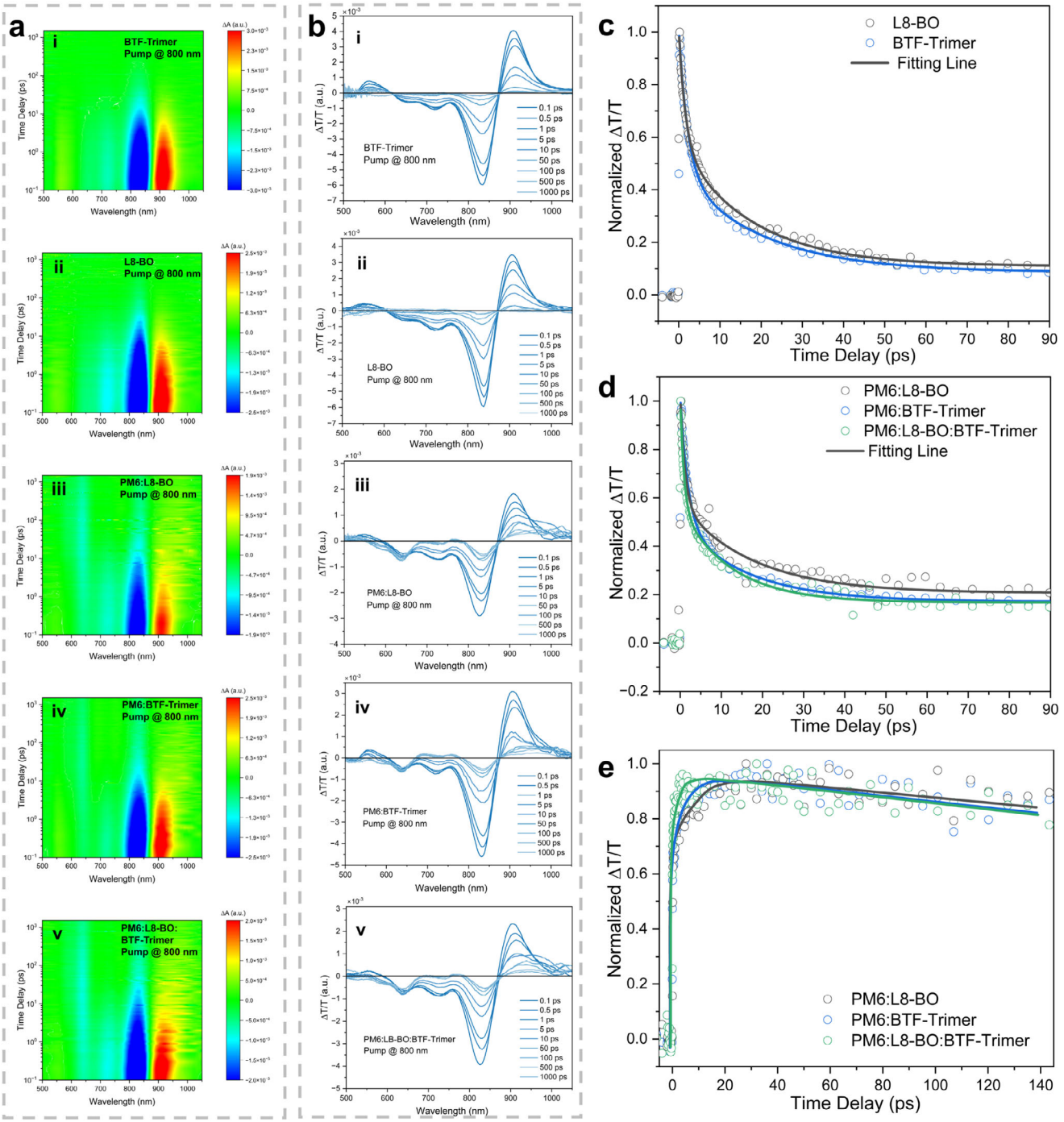

Figure 4. Exciton and charge carrier dynamics. ai–v) 2D TAs images and bi–v) the corresponding spectra of neat and blend films excited at 800 nm. Normalized decay curves of GSB signals probed at 834 nm for c) the L8-BO and BTF-Trimer neat films and d) the blend films. e) Normalized decay curves of GSB signals probed at 640 nm for the blend films.

exciton (DSE) state, which is a critical intermediate state from the LE to the charge-separated states, facilitating the exciton dissociation and the generation of free charges.[48] In addition, a new GSB signal ascribed to PM6 emerged at 600–650 nm and rised rapidly in the first 10–30 ps. Since the blend films were excited exclusively for the acceptors, the appearance of PM6 GSB signals testifies the efficient hole transfer (HT) from the acceptors to donors. Specifically, as shown in Figure 4e, the intensity of GSB signals for PM6:L8-BO:BTF-Trimer reached the peak within 13.65 ps, much faster than the L8-BO-based (28.16 ps) and BTF-Trimer-based binary films (18.30 ps), indicative of highly effective HT process ascribed to the optimal morphology and the increased D/A interfaces as discussed in previous sections.

To further elucidate the disparate impacts of trimerization and L8-BO on charge recombination in the active layer, the exited state evolutions for each sample were derived from the singular-value-decomposition (SVD) fittings of the TAs profiles, as shown in Figures S14 and S15 (Supporting Information).[49] For neat L8-BO and BTF-Trimer films as shown in Figure S14 (Supporting Information), the 834 nm GSB signal and the two 560/908 nm ESA signals depicted a fast decay process in 5.68 and 2.82 ps, respectively, standing for the fast exciton annihilations process.[50] These signals were then decayed significantly within 168.3 and 37.23 ps, as illustrated by the other component, and such rapid decay of excited charges can be attributed to germination recombination, which is often the case for Y-series NFAs.[51] It is noticed that the exciton germination recombination rate of L8-BO is slower than that of BTF-Trimer, which is mainly caused by its more refined crystal structure. With regards to the blend films, as shown in Figure S15 (Supporting Information), both binary films displayed similar characteristics in the first two components (≈19 ps), with the concurrent negative and positive bands at 800–850 and 600–650 nm, suggesting a two-step mediated HT from acceptors to donors, where an intermediate charge-transfer state (CTS) was formed after the hole injection and subsequently dissociated to the excited holes.[52] This process is different in ternary blend films, wherein the second component was obviously slower than that of a binary system with remaining negative signals at 800–850 nm but negative signals at 600–650 nm, indicative of direct and efficient hole transfer after exciton dissociation without forming an intermediate. In the third or more components of binary and ternary systems, the two GSB and two ESA signals peaked at ≈637/834 nm and ≈750/904 nm represented the process of bimolecular recombination of the photogenerated free carriers. It was found that the bimolecular recombination time was remarkably extended from 338.70 ps to 1.667 ns for BTF-Trimer- and L8-BO-based binary blend films, and further increased to >3 ns after adding BTF-Trimer into the PM6:L8-BO, indicative of the suppressed bimolecular recombination and the prolonged charge carrier lifetime in ternary blend films. Complementarily, we also conducted the TAs measurements pumped at 400 nm to selectively excite the donors as shown in Figures S16–S18 (Supporting Information). It was unveiled that similar to the results of 800 nm excitation, the ternary blend films presented the fastest electron transfer (5.58 ps) and the efficient exciton diffusion/dissociation ($\tau_1 = 2.5$ ps / $\tau_2 = 35.7$ ps). This is due to the optimal D/A phases with suitable aggregation size and better phase continuity as evidenced in Section 2.3, facilitating exciton dissociation and charge transport.

In addition to the TAs measurements, we also calculated the exciton generation contour from FLAS to in-depth illustrate the exciton generation process as shown in Figure S19a–c (Supporting Information). The FLAS results show that the BTF-Trimer-treated ternary films exhibited superior exciton generation rates to binary films within both the donor (300–600 nm) and acceptor (700–900 nm) absorption regions. As depicted in Figure S19d–f (Supporting Information), the ternary films achieved the highest peak exciton generation rate of 19 versus 17 cm^{-3} s^{-1} in binary counterparts, suggesting the formation of more photogenerated excitons, which is favored to elevate photocurrents in devices.

2.5. Thermal Stress and Storage Stabilities

Finally, we tested the storage and thermal stabilities, both of which are critical for practical applications. **Figure 5a,b** present the testing results of the unencapsulated devices under conditions of room temperature in an Ar atmosphere and 70 °C in an air environment, respectively. Note that these devices were fabricated by the PEDOT:PSS HTL, and therefore their stabilities were negatively impaired by the degradation of the transport layer. For the storage stabilities, the PCEs of both binary and ternary devices displayed a dramatic decrease in the first 150 h, which is attributed to the degradation of the PEDOT:PSS. After aging 1000 h, the PM6:L8-BO-based devices suffered from a significantly dropped PCE to less than 70% of its initial value, with a T_{70} (the time required to reach 70% of the initial efficiency) lifetime of 727 h. However, when the BTF-Trimer was introduced into host PM6:L8-BO binary films, the decline in PCEs became apparently steady, with remaining ≈80% initial PCE after aging 1000 h and achieving an extrapolated T_{70} lifetime of 2793 h, indicative of an excellent storage stability of PM6:L8-BO:BTF-Trimer-based devices. Meanwhile, we also evaluated the thermal stabilities of both binary and ternary devices in air condition. As shown in Figure 5b, all the devices exhibited rapid degradation in the presence of heat and water-oxygenation, especially L8-BO-based binary devices, with PCE rapidly dropping below 70% in 50 h. In contrast, binary or ternary devices containing BTF-Trimer displayed a relatively mild downward trend, with remaining ≈70% initial PCE after aging for 150 h, suggesting enhanced thermal stabilities. To rationalize the positive effect of BTF-Trimer on stabilities, we evaluated the T_gs of acceptors by measuring their UV–vis absorption in solid films at different temperatures, which play a crucial role in maintaining stable micro-scale morphologies.[53] The deviation metrics (DMT) of the absorption of both acceptor films were calculated and plotted against the annealing temperature, and the T_gs were identified where two fitted lines were intersected as illustrated in Figure 5c,d. The three-armed BTF-Trimer exhibited a significantly higher T_g of 157 °C than the small molecule L8-BO (104 °C), which could be attributed to the favorable effect of suppressing molecular diffusion and stabilizing film morphology for BTF-Trimer due to its huge chemical structure and high molecular weight. Based on the calculated T_g, the diffusion coefficients (D_{85}) of BTF-Trimer and L8-BO were estimated to be 1.14×10^{-21} and 3.24×10^{-18} cm^2 s^{-1}, respectively, according to the equation $D_{85} = 1.2 \times 10^7 e^{-0.15 T_g}$. This confirms the slower diffusion process of BTF-Trimer, thereby enhancing the storage and thermal stabilities.

Additionally, we conducted the AFM characterizations to directly showcase the morphological evolutions of the acceptor-only and blend films as displayed in Figures 5e,f and S20 (Supporting Information). Owing to the inhibition molecular diffusion, after aging for 500 h, BTF-Trimer films exhibited no significant self-aggregation and maintained a relatively homogeneous surface morphology whereas L8-BO films showed large aggregation clusters and increased RMS. These characteristics were preserved in the blend films (Figure S20, Supporting Information), where the PM6:L8-BO:BTF-Trimer ternary blend films displayed relatively smaller phase-separation and smoother surface than the PM6:L8-BO-based analogs, indicating the reinforced

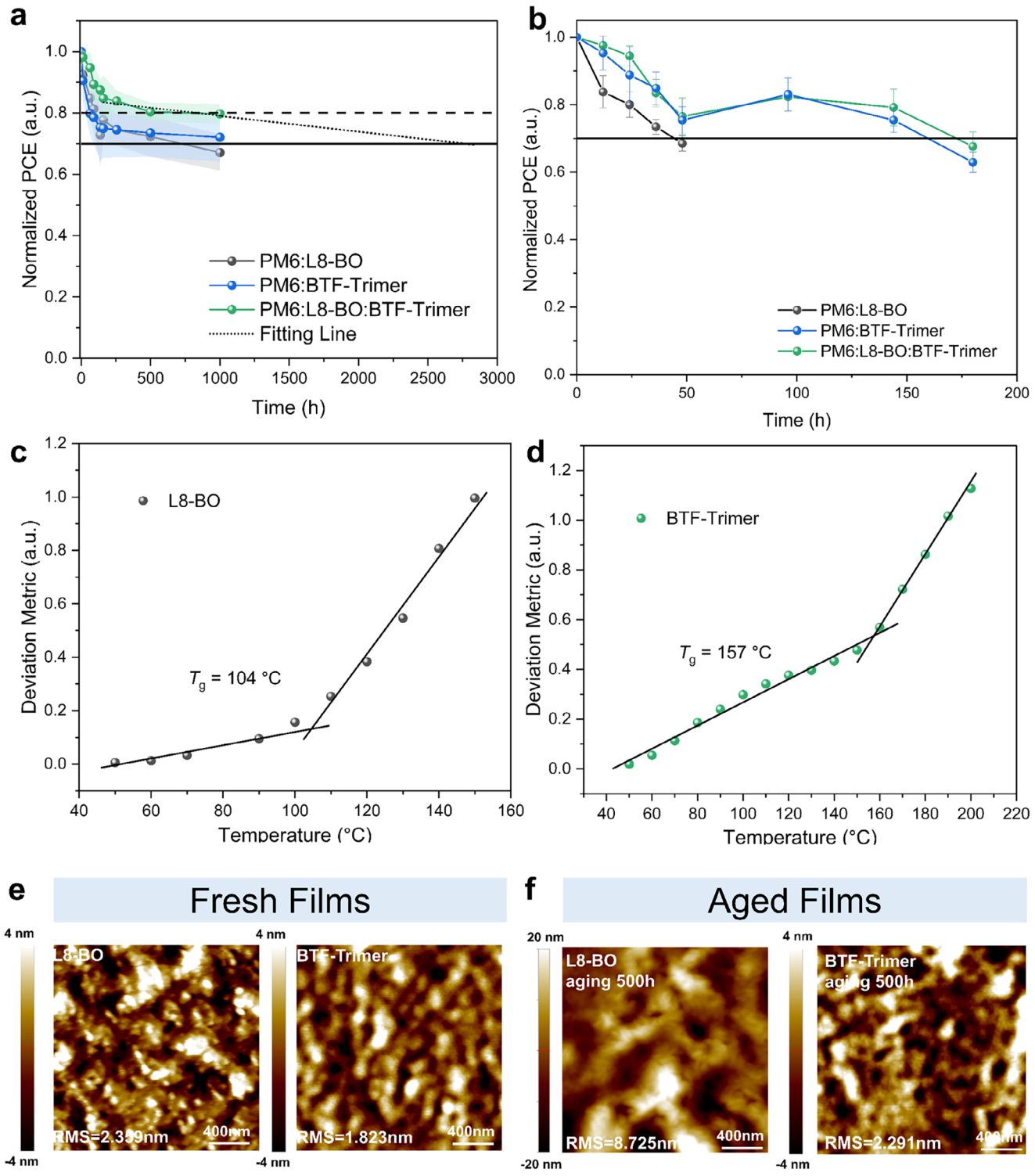

Figure 5. Stability analysis. a) Storage stabilities of the unencapsulated devices in Ar atmosphere. b) Thermal stabilities of the unencapsulated devices stored under 70 °C in air condition. Plots of the DMT of c) L8-BO and d) BTF-Trimer films as a function of annealing temperature. TP-AFM height images of e) fresh and f) aged L8-BO and BTF-Trimer thin film in Ar atmosphere.

morphology stability in consistence with the elongated device lifetime.

3. Conclusion

To conclude, we have developed a new star-shaped trimeric acceptor BTF-Trimer connecting a BTF core with three Y-OD acceptor units. BTF-Trimer demonstrated a non-planar molecular conformation yet featured multi-directional electron transport channels, resulting in attenuated aggregation but commendable electron transport capabilities. Upon incorporation of BTF-Trimer into the benchmark PM6:L8-BO binary system, the excessive aggregation of L8-BO acceptors was suppressed and the compatibility between donor and acceptor was enhanced, yielding a dual-fibril interpenetrating network morphology, which facilitated exciton dissociation and hole transfer. Noticeably, the bimolecular recombination was unveiled to be significantly inhibited in the ternary blend films and devices. These advantageous effects collectively contributed to an elevation of PCEs from 17.35% in binary devices to 18.17% in ternary ones, further increasing to 19.13% with a 2PACz HTL. Moreover, by virtue of the high T_g and low D_{85} of the star-shaped BTF-Trimer, the long-term stabilities were bolstered under storage and thermal conditions. This study highlights the paradox of phase size and continuity of nonfullerene photovoltaics, which can be effectively resolved by star-shaped trimer acceptors, boosting both the efficiency and stability.

Supporting Information

Supporting Information is available from the Wiley Online Library or from the author.

Acknowledgements

The work was financially supported by Shanghai Leading Talent Program of Eastern Talent Plan and the National Natural Science Foundation of China (NSFC) under grant No. 22375050. The authors gratefully thank for the beam time and technical support provided by the BL03HB GIWAXS beamline at Shanghai Synchrotron Radiation Facility (SSRF). The authors also would thank Dr. Kaibo Zheng a lot from Lund University and SCI-GO (https://www.sci-go.com) for the TAs measurements and the MALDI-TOF-MS testing, respectively.

Conflict of Interest

The authors declare no conflict of interest.

Author Contributions

Z.W. conducted the experiments and wrote the manuscript under the supervision of Z.L. W.W. conducted the NMR characterization of the monomers under the supervision of H.Q. W.W. and H.Q. offered valuable suggestions for the synthesis of monomer and the manuscript. Z.L. led the project and provided a guide to the manuscript. All authors discussed the results and commented on the manuscript.

Data Availability Statement

The data that support the findings of this study are available from the corresponding author upon reasonable request.

Keywords

charge transfer, exciton dissociation, morphology mediation, organic solar cells, star-shaped trimeric acceptor

Received: March 12, 2025
Revised: April 17, 2025
Published online: May 7, 2025

[1] J. Wang, P. Xue, Y. Jiang, Y. Huo, X. Zhan, *Nat. Rev. Chem.* **2022**, *6*, 614.
[2] H. Yu, J. Wang, Q. Zhou, J. Qin, Y. Wang, X. Lu, P. Cheng, *Chem. Soc. Rev.* **2023**, *52*, 4132.
[3] S. Rasool, J. W. Kim, H. W. Cho, Y. J. Kim, D. C. Lee, C. B. Park, W. Lee, O. H. Kwon, S. Cho, J. Y. Kim, *Adv. Energy Mater.* **2022**, *13*, 2203452.
[4] L. Zhu, M. Zhang, G. Zhou, Z. Wang, W. Zhong, J. Zhuang, Z. Zhou, X. Gao, L. Kan, B. Hao, F. Han, R. Zeng, X. Xue, S. Xu, H. Jing, B. Xiao, H. Zhu, Y. Zhang, F. Liu, *Joule* **2024**, *8*, 3153.
[5] J. Zhou, L. Wang, C. Liu, C. Guo, C. Chen, Y. Sun, Y. Yang, J. Cheng, Z. Gan, Z. Chen, W. Sun, J. Zhou, W. Xia, D. Liu, W. Li, T. Wang, *J. Am. Chem. Soc.* **2024**, *146*, 34998.
[6] X. Kong, N. Yang, X. Zhang, J. Zhang, Z. Li, X. Li, Y. Wu, R. Sun, J. Li, A. Li, J. Min, G. Yang, C. Sun, *Energy Environ. Sci.* **2025**, *18*, 386.
[7] X. Zhou, W. Liang, R. Ma, C. Zhang, Z. Peng, T. A. Dela Peña, J. Wu, Z. Ma, Y. Liao, G. Li, H. Hu, *Energy Environ. Sci.* **2024**, *17*, 7762.
[8] Z. Zhang, Q. Chen, C. Zhang, W. L. Tan, G. Zhang, Z. Bu, C. Xiao, X. Shen, Z. Tang, C. R. McNeill, W. Li, *Adv. Funct. Mater.* **2024**, *34*, 2401823.
[9] S. Yadav, M. Pranav, C. Gangadharappa, M. Huss-Hansen, M. Schwartzkopf, J. Kjelstrup-Hansen, M. Knaapila, S. Patil, *ACS Energy Lett.* **2024**, *9*, 5259.
[10] P. Ding, D. Yang, S. Yang, Z. Ge, *Chem. Soc. Rev.* **2024**, *53*, 2350.
[11] H. Xu, J. Han, A. Sharma, S. H. K. Paleti, S. Hultmark, A. Yazmaciyan, C. Müller, D. Baran, *Adv. Mater.* **2024**, *37*, 2407119.
[12] Y. Liang, D. Zhang, Z. Wu, T. Jia, L. Lüer, H. Tang, L. Hong, J. Zhang, K. Zhang, C. J. Brabec, N. Li, F. Huang, *Nat. Energy* **2022**, *7*, 1180.
[13] X. Gu, X. Zhang, H. Huang, *Angew. Chem., Int. Ed.* **2023**, *62*, 202308496.
[14] S. Li, R. Zhang, M. Zhang, J. Yao, Z. Peng, Q. Chen, C. Zhang, B. Chang, Y. Bai, H. Fu, Y. Ouyang, C. Zhang, J. A. Steele, T. Alshahrani, M. B. J. Roeffaers, E. Solano, L. Meng, F. Gao, Y. Li, Z. G. Zhang, *Adv. Mater.* **2022**, *35*, 2206563.
[15] J.-W. Lee, C. Sun, C. Lee, Z. Tan, T. N.-L. Phan, H. Jeon, D. Jeong, S.-K. Kwon, Y.-H. Kim, B. J. Kim, *ACS Energy Lett.* **2023**, *8*, 1344.
[16] J. W. Lee, J. S. Park, H. Jeon, S. Lee, D. Jeong, C. Lee, Y. H. Kim, B. J. Kim, *Chem. Soc. Rev.* **2024**, *53*, 4674.
[17] H. Zhuo, X. Li, J. Zhang, C. Zhu, H. He, K. Ding, J. Li, L. Meng, H. Ade, Y. Li, *Nat. Commun.* **2023**, *14*, 7996.
[18] Q. Zhang, H. Gao, L. Li, Y. Shen, M. Zuo, G. Lu, X. Wu, Y. Han, *Adv. Energy Mater.* **2025**, *15*, 2404507.
[19] C. Zhang, X. Zhong, X. Sun, J. Lv, Y. Ji, J. Fu, C. Zhao, Y. Yao, G. Zhang, W. Deng, K. Wang, G. Li, H. Hu, *Adv. Sci.* **2024**, *11*, 2401313.
[20] Y. Wang, H. Gao, M. Sun, C. T. Lin, H. Li, F. R. Lin, B. Fan, Z. Li, J. A. Zapien, A. K. Y. Jen, *Adv. Energy Mater.* **2024**, *14*, 2304449.
[21] M. Zhang, Z. Wang, L. Zhu, R. Zeng, X. Xue, S. Liu, J. Yan, Z. Yang, W. Zhong, G. Zhou, L. Kan, J. Xu, A. Zhang, J. Deng, Z. Zhou, J. Song, H. Jing, S. Xu, Y. Zhang, F. Liu, *Adv. Mater.* **2024**, *36*, 2407297.
[22] X. Ding, X. Wu, S. Li, T. Chen, J. Yu, H. Liu, M. Wang, X.-K. Ye, N. Zhang, X. Lu, C.-Z. Li, H. Zhu, M. Shi, H. Li, H. Chen, *Energy Environ. Sci.* **2025**, *18*, 948.

[23] M. Zhang, B. Chang, R. Zhang, S. Li, X. Liu, L. Zeng, Q. Chen, L. Wang, L. Yang, H. Wang, J. Liu, F. Gao, Z. G. Zhang, *Adv. Mater.* **2023**, *36*, 2308606.
[24] H. Gao, B. Fan, L. Yu, Y. Wang, R. Li, W. Jiang, T. Chen, J. Zeng, F. R. Lin, B. Kan, H. Li, L. Wang, A. K. Y. Jen, *ACS Energy Lett.* **2024**, *9*, 5541.
[25] P. Ding, Z. Chen, D. Yang, X. Yu, J. Shi, Y. Chen, J. Zhu, J. Wu, X. Cao, L. Xie, F. Chen, Z. Ge, *Adv. Mater.* **2024**, *37*, 2414080.
[26] H. Zhuo, B. Qiu, X. Li, Z.-G. Zhang, Y. Li, *Giant* **2024**, *20*, 100336.
[27] P. Tan, H. Chen, H. Wang, X. Lai, Y. Zhu, X. Shen, M. Pu, H. Lai, S. Zhang, W. Ma, F. He, *Adv. Funct. Mater.* **2023**, *34*, 2305608.
[28] Y. Bai, T. Chen, X. Ji, J. Wang, W. Zhao, S. Yuan, Y. Zhang, G. Long, Z. Zhang, X. Wan, B. Kan, Y. Chen, *Adv. Energy Mater.* **2024**, *14*, 2400938.
[29] H. Fu, Q. Wang, Q. Chen, Y. Zhang, S. Meng, L. Xue, C. Zhang, Y. Yi, Z. G. Zhang, *Angew. Chem., Int. Ed.* **2024**, *63*, 202403005.
[30] J. Ji, L. Zhu, X. Xiong, F. Liu, Z. Liang, *Adv. Sci.* **2022**, *9*, 2200864.
[31] C. Wang, X. Ma, Y.-f. Shen, D. Deng, H. Zhang, T. Wang, J. Zhang, J. Li, R. Wang, L. Zhang, Q. Cheng, Z. Zhang, H. Zhou, C. Tian, Z. Wei, *Joule* **2023**, *7*, 2386.
[32] W. Liu, X. Xu, S. He, R. Sun, Q. Chen, J. Min, Z. Zhang, J. Yuan, Y. Li, Y. Zou, *Macromolecules* **2023**, *56*, 8623.
[33] J. W. Lee, C. Sun, J. Lee, D. J. Kim, W. J. Kang, S. Lee, D. Kim, J. Park, T. N. L. Phan, Z. Tan, F. S. Kim, J. Y. Lee, X. Bao, T. S. Kim, Y. H. Kim, B. J. Kim, *Adv. Energy Mater.* **2024**, *14*, 2303872.
[34] B. Chang, Y. Zhang, C. Zhang, M. Zhang, Q. Wang, Z. a. Xu, Q. Chen, Y. Bai, H. Fu, S. Meng, L. Xue, S. Kim, C. Yang, Y. Yi, Z. G. Zhang, *Angew. Chem. Int. Ed.* **2024**, *63*, 202400590.
[35] Z. Xu, S. Li, F. Huang, T. He, X. Jia, H. Liang, Y. Guo, G. Long, B. Kan, Z. Yao, C. Li, X. Wan, Y. Chen, *Angew. Chem. Int. Ed.* **2023**, *62*, 202311686.
[36] C. Sun, J. Wang, F. Bi, H. Jiang, C. Yang, Y. Li, J. Chu, X. Bao, *Energy Environ. Sci.* **2025**, *18*, 862.
[37] H. Zhuo, X. Li, S. Qin, J. Zhang, Y. Gong, Y. Wu, T. Zou, Z. Chen, K. Yin, M. Yuan, J. Li, L. Meng, Y. Li, *Adv. Funct. Mater.* **2024**, *34*, 2410092.
[38] J. Ji, Z. Wu, J. Xie, W. Wang, H. Qian, Z. Liang, *Adv. Mater.* **2024**, *36*, 2313237.
[39] W. Zhou, J. Liu, J. Xie, S. You, J. Deng, F. Yu, S. Y. Jeong, H. Y. Woo, F. Wu, L. Chen, *Angew. Chem. Int. Ed.* **2024**, *64*, 202415141.
[40] F. Yang, H. Fang, E. Guo, C. Xiao, Z. Lu, Y. Wang, H. Fan, A. Zhang, W. Lai, W. Li, *Angew. Chem. Int. Ed.* **2025**, *64*, 202501302.
[41] M. J. Frisch, G. W. Trucks, H. B. Schlegel, G. E. Scuseria, M. A. Robb, J. R. Cheeseman, G. Scalmani, V. Barone, G. A. Petersson, *Gaussian 16, Revision A.03*, Gaussian, Inc, Wallingford CT, **2016**.
[42] C. Chen, L. Wang, Y. Sun, Y. Fu, C. Guo, B. Zhou, Z. Gan, D. Liu, W. Li, T. Wang, *Adv. Funct. Mater.* **2023**, *33*, 2305765.
[43] J. Cheng, C. Guo, L. Wang, Y. Fu, D. Li, C. Chen, Z. Gan, Y. Sun, D. Liu, W. Li, T. Wang, *Joule* **2024**, *8*, 2250.
[44] D. K. Owens, R. C. Wendt, *J. Appl. Polym. Sci.* **1969**, *13*, 1741.
[45] T. Wang, J.-L. Brédas, *J. Am. Chem. Soc.* **2021**, *143*, 1822.
[46] M. Sumita, K. Sakata, S. Asai, K. Miyasaka, H. Nakagawa, *Polym. Bull.* **1991**, *25*, 265.
[47] D. Li, A. W. Neumann, *J. Colloid Interface Sci.* **1990**, *137*, 304.
[48] S. Y. Shi, C. Yang, X. Xu, Z. X. Liu, W. Duan, X. X. Chen, Z. Lu, H. Zhou, Z. P. Yu, C. Z. Li, *Angew. Chem. Int. Ed.* **2024**, *64*, 202415994.
[49] J. Xie, W. Lin, G. C. Bazan, T. Pullerits, K. Zheng, Z. Liang, *J. Mater. Chem. A* **2022**, *10*, 18845.
[50] M. G. Lo Gerfo, L. Bolzonello, F. Bernal-Texca, J. Martorell, N. F. van Hulst, *J. Phys. Chem. Lett.* **2023**, *14*, 1999.
[51] D. Baran, N. Gasparini, A. Wadsworth, C. H. Tan, N. Wehbe, X. Song, Z. Hamid, W. Zhang, M. Neophytou, T. Kirchartz, C. J. Brabec, J. R. Durrant, I. Mcculloch, *Nat. Commun.* **2018**, *9*, 2059.
[52] J. Xie, W. Lin, D. Wang, Z. H. Lu, K. Zheng, Z. Liang, *Adv. Funct. Mater.* **2023**, *34*, 2309511.
[53] S. E. Root, M. A. Alkhadra, D. Rodriquez, A. D. Printz, D. J. Lipomi, *Chem. Mater.* **2017**, *29*, 2646.